Supraphysiologic Testosterone Induces Ferroptosis and Activates Immune Pathways through Nucleophagy in Prostate Cancer

Rajendra Kumar[1], Janet Mendonca[1], Olutosin Owoyemi[1], Kavya Boyapati[1], Naiju Thomas[1],
Suthicha Kanacharoen[1], Max Coffey[1], Deven Topiwala[1], Carolina Gomes[1], Busra Ozbek[1], Tracy Jones[1],
Marc Rosen[1], Liang Dong[1], Sadie Wiens[2], W. Nathaniel Brennen[1], John T. Isaacs[1], Angelo M. De Marzo[1],
Mark C. Markowski[1], Emmanuel S. Antonarakis[1], David Z. Qian[2], Kenneth J. Pienta[1], Drew M. Pardoll[1],
Michael A. Carducci[1], Samuel R. Denmeade[1], and Sushant K. Kachhap[1]

ABSTRACT

The discovery that androgens play an important role in the progression of prostate cancer led to the development of androgen deprivation therapy (ADT) as a first line of treatment. However, paradoxical growth inhibition has been observed in a subset of prostate cancer upon administration of supraphysiologic levels of testosterone (SupraT), both experimentally and clinically. Here we report that SupraT activates cytoplasmic nucleic acid sensors and induces growth inhibition of SupraT-sensitive prostate cancer cells. This was initiated by the induction of two parallel autophagy-mediated processes, namely, ferritinophagy and nucleophagy. Consequently, autophagosomal DNA activated nucleic acid sensors converge on NFκB to drive immune signaling pathways. Chemo-

kines and cytokines secreted by the tumor cells in response to SupraT resulted in increased migration of cytotoxic immune cells to tumor beds in xenograft models and patient tumors. Collectively, these findings indicate that SupraT may inhibit a subset of prostate cancer by activating nucleic acid sensors and downstream immune signaling.

Significance: This study demonstrates that supraphysiologic testosterone induces two parallel autophagy-mediated processes, ferritinophagy and nucleophagy, which then activate nucleic acid sensors to drive immune signaling pathways in prostate cancer.

Introduction

In 1941, Charles Huggins discovered the benefits of androgen deprivation therapy (ADT), which has become the mainstay for advanced prostate cancer treatment (1). However, from the outset, it was recognized that all men eventually develop castration-resistant prostate cancer (CRPC; ref. 2). Evaluation of clinical specimens demonstrates that CRPC cells remain highly reliant on androgen receptor (AR) signaling (3, 4). These studies suggested that the adaptive reliance on AR signaling by CRPC cells becomes a therapeutic liability that can be exploited through the administration of supra-physiologic levels of testosterone (SupraT), a concept we have termed bipolar androgen therapy (BAT; refs. 5, 6). In this regard, we and others have demonstrated that the growth of some AR-positive human prostate cancer cells can be inhibited by exposure to SupraT (6). The

mechanisms underlying this paradoxical effect of SupraT on prostate cancer cells are likely multifactorial as the androgen is the key mediator of prostate cancer cell metabolism, proliferation, and death. Haffner and colleagues and others showed that androgens generate double-strand DNA breaks (DSB) in prostate cancer cells through the recruitment of AR and topoisomerase II beta to androgen response elements (7, 8). Hypothetically, in prostate tumors with DNA repair mutations, SupraT-induced DSBs would trigger DNA repair stress and lead to either growth inhibition or cell death (9). Intuitively, these tumors would be acutely susceptible to BAT. In agreement with this postulate, we have recently discovered an association between germ-line and/or somatic DNA repair gene mutations and favorable response to BAT (10–12). A link between DNA repair gene mutation or transcriptome repression and response to BAT has also been reported by others (9, 13). In this study, we report SupraT induces ferroptosis and nucleophagy-mediated immune activation, resulting in growth inhibition of prostate cancer.

[1]The Sidney Kimmel Comprehensive Cancer Center, Johns Hopkins University School of Medicine, Baltimore, Maryland. [2]OHSU Knight Cancer Institute, Prostate Cancer Program, Portland, Oregon.

Corresponding Author: Sushant K. Kachhap, The Sidney Kimmel Comprehensive Cancer Center, Johns Hopkins University, 1650 Orleans Street, CRB-1M53, Baltimore, MD 21231. Phone: 410-502-6489; Fax: 410-367-2667; E-mail: kachhsu@jhmi.edu

Materials and Methods

Cell culture

LNCaP, LAPC4, HEK293T, and NK92 cells were purchased from the ATCC. LNCaP, LAPC4, and 22Rv1 cells were cultured in phenol red–free RPMI (Thermo Fisher Scientific), and HEK293T cells were cultured in DMEM-high glucose (Sigma) supplemented with 10% FBS (Gemini Bio). VCaP cells were cultured in DMEM media (ATCC) containing 1.5 g/L sodium bicarbonate. NK92 cells were cultured in CTS AIM V SFM (Thermo Fisher Scientific) with 200 U/mL recombinant IL2 (Peprotech), 12.5% horse serum (Thermo Fisher Scientific), and 12.5% FBS according to manufacturer's instructions. All cell lines

were tested for *Mycoplasma* using the PCR-based *Mycoplasma* detection kit (Agilent).

Knockout/knockdown cell line generation

To generate the gene knockouts, tetracycline induced *cas9* vector (Addgene # 50661) was stably expressed in prostate cancer lines. Single-guide RNAs (sgRNA) against target genes given in were cloned in pLXsgRNA vector (Addgene# 50662), and lentiviral particles for sgRNA were produced in HEK293T cells by cotransfecting pLXsgRNA plasmid with pMD2.G (Addgene# 12259) and psPAX2 (Addgene #12260; Supplementary Table S1A) Viruses were harvested after 48 hours, and cells were infected with lentiviral particles. Transduced cells were treated with 1 μg/mL doxycycline to induce *cas9* before selection with 10 μg/mL blasticidin. Following selection, cells were transferred in 96-well plates to select individual clones. Knockouts were verified by Western blots, and confirmed clones were expanded and cryopreserved for future experiments.

For NCOA4 knockdown in LNCaP cells, MISSION short hairpin RNA (shRNA) constructs (TRCN0000236184, TRCN0000236186, TRCN0000236187, TRCN0000236188, and TRCN000019724) were purchased from Sigma, and lentiviral particles were generated in HEK293T cells by cotransfecting shRNA plasmid construct with pMD2.G (Addgene#12259) and psPAX2 (Addgene#12260). LNCaP cells were infected with NCOA4 lentivirus and were selected with 1.0 μg/mL puromycin. The level of NCOA4 knockdown was measured by Western blots, and confirmed cells were expanded, cryopreserved, and used for the experiments.

Quantitative real-time PCR

Total RNA was extracted from cells using TRIzol reagent (Thermo Fisher Scientific) as per manufacturer's instructions. cDNA was synthesized from RNA by reverse transcription using SuperScript IV reverse (Thermo Fisher Scientific). Quantitative PCR was performed on samples mixed with SYBR master mix (Bio-Rad) and gene-specific primers using a real-time thermocycler (Bio-Rad). Data analysis was performed using the $\Delta\Delta C_t$ method, and fold change ($2^{-\Delta\Delta C_t}$) was calculated after double normalization with the housekeeper gene and respective untreated control. Each PCR reaction was run in triplicates. Details of primer sequences used in quantitative PCR are provided in Supplementary Table S1B.

Immunoprecipitation

NCOA4-FLAG-HA (CTAP) plasmid was received as a gift from J Wade Harper (Harvard Medical School, Boston, MA). LNCaP cells were transfected with NCOA4-FLAG plasmid for immunoprecipitation studies or kept as untransfected control (C). NCOA4-FLAG–transfected cells were either treated with 10 nmol/L R1881 (T) or kept as untreated control (C*). Following treatment, cells were washed with 3 mL PBS, harvested in ice-cold PBS, and pelleted using a refrigerated centrifuge. Cells were lysed with 750 μL 1× lysis buffer (Promega) containing protease and phosphatase inhibitor for 20 minutes on ice. After lysis, the lysates were centrifuged at 13,200 × *g* at 4°C, and 10% of supernatant was stored as input. The remaining supernatant was used for immunoprecipitation using anti-FLAG M2 agarose beads (Thermo Fisher Scientific) as per manufacturer's instructions. Affinity separated FLAG-tagged protein was eluted using 35 μL IgG elution buffer (Thermo Fisher Scientific), denatured with an equal volume of Laemmli buffer, and stored at −80°C before Western blot analysis. Each experiment was repeated at least three times.

Western blotting

Cell lysates were prepared either in 1× denaturing lysis buffer (Cell Signaling Technology, #9803) or non-denaturing lysis buffer (50 mmol/L HEPES pH 7.4, 150 mmol/L NaCl, 5 mmol/L EDTA, 10% glycerol, 1% Nonidet P-40, and supplemented with phosphatase and protease inhibitors). For denaturing gels, lysates were mixed with Laemmli buffer containing β-mercaptoethanol, boiled for 5minutes and stored at −80°C until use. Native lysates were mixed with native loading buffer (Bio-Rad), and semi-native lysates were mixed with Laemmli buffer without β-mercaptoethanol and stored at −80°C without boiling. Native gels were resolved as described previously (14); denaturing and semi-native gels were resolved on 4%–15% precast polyacrylamide gels (Bio-Rad) followed by transfer to polyvinylidene difluoride membrane. Membranes were blocked in 5% nonfat milk in wash buffer (TBS + 0.1% Tween-20). After blocking, immunoblotting was performed with primary antibodies overnight at 4°C, followed by incubation with horseradish peroxidase–conjugated secondary antibodies for 1 hour at room temperature. Blots were analyzed using the chemiluminescence method. Blots were developed using ECL Western blot detection reagent (GE Healthcare) for highly expressed proteins and Super Signal West Femto (Thermo Fisher Scientific) reagent for low expression proteins. Each experiment was repeated at least two to three times. The antibodies used are listed in Supplementary Table S2.

Immunofluorescence

Cells were grown on sterile coverslips in low density and were treated with R1881 (T) or vehicle control (C). After treatment, media was removed, and cells were fixed and permeabilized using chilled methanol for 10 minutes in deep freezer followed by 10 minutes fixation in 10% natural buffered formalin (NBF) at room temperature. Post-fixation, cells were blocked overnight in sterile-filtered 5% BSA in PBS at 4°C. Cells were incubated with a primary antibody, followed by a suitable fluorochrome-tagged secondary antibody at 4°C overnight. Both primary and secondary antibodies were diluted with 5% BSA in PBS. Cells were postfixed with 10% NBF for 2–3 minutes before mounting on a clean glass slide using Vectashield antifade mounting media (Vector Laboratories). Image acquisition was performed on the LSM 700 laser confocal microscope (Zeiss). Experiment was repeated at least three times and images from at least five random fields from each experiment were used for analysis. Images were analyzed using the image processing package Fiji.

Measurement of cell death

Cells were stained with 0.4% trypan blue (Sigma) and incubated for 2–3 minutes at room temperature to allow dead cells to take up the blue stain. Cell viability was measured using an automated cell counter, Cellometer (Nexcelom). Each experiment was repeated at least three times. Dead cells were calculated from subtracting the percentage of viable cells from 100. Mean percentage of dead cells was plotted on histograms.

Measurement of the labile iron pool (Fe^{2+})

An iron assay kit (Sigma) was used to measure the labile iron pool in control and R1881-treated cells. LNCaP and LAPC4 cells were culture in a 100 mm tissue culture dish and were treated for 72 hours before lysis in the buffer provided with the kit by snap freezing and thawing method. The lysate was cleared by centrifuging at 13,000 × *g*, and iron was measured by iron detection reagents supplied in the kit. Iron levels were calculated and normalized by the total protein present in the cell lysate. Levels of Fe^{2+} were analyzed in SupraT-treated cells and were normalized to vehicle control cells.

Natural killer cell migration assay

This assay was performed in a transwell coculture setup, using tumor cells in the bottom chamber (culture plate) and NK-92 cells in the upper chamber (insert; Corning). LNCaP and LAPC4 cells were first seeded in a 24-well plate for 24 hours (day 1). The following day, tumor cells were treated with vehicle (C) or 10 nmol/L R1881 (T) for 72 hours. After 72 hours, NK-92 cells, stained with 5 μmol/L CFSE (BioLegend) for 10 minutes at 37°C, were then added to a 5-μm pore size insert placed in each culture well already containing the vehicle/R1881-treated tumor cells. The culture plate was incubated for 6 hours, and microscopy was performed to image the CFSE-labeled NK-92 cells that migrated to the lower chamber of the plate. Images were analyzed using the Image J software to determine the cell count. At least five fields were counted per experiment.

Cell-cycle analysis

Harvested cell pellets were resuspended in ice-cold 70% ethanol and incubated at −20°C overnight. Cells were then washed with 1× PBS, resuspended in 50 μg/mL propidium iodide (Sigma) in PBS with 50 μg/mL RNase A (Sigma), and incubated for 30 minutes at room temperature. Cell-cycle analysis was performed using BD FACSCelesta cytometer equipped with BD FACS DIVA. Data were analyzed using the FlowJo software version 10 (FlowJo). The distribution of cells in the cell-cycle phases was calculated using the Watson-Pragmatic algorithm. Each experiment was repeated at least three times.

NanoString immune profiling assay

Total RNA was isolated from vehicle/R1881-treated cells using TRIzol (Thermo Fisher Scientific), and RNA quality was determined using the Bioanalyzer (Agilent). Gene signature was determined by using the NanoString PanCancer Immune Profiling Panel according to the manufacturer's instructions (NanoString Technologies). Housekeeping genes and built-in positive controls were used for data normalization and quality control assessments. Data analysis and gene expression analysis was performed using the nSolver 4.0 software (NanoString Technologies).

Luciferase reporter assay

Dual-luciferase reporter assay (Promega) was used to measure NFκB, STING, and AIM-2 promoter activity. LNCaP and LAPC4 cells were transfected with Ig-IFN-Luc and Renila-Luc plasmids in 12-well plates and were incubated with vehicle or 10 nmol/L R1881 treatment for 72 hours. Post-treatment, cells were washed with PBS, followed by lysis with 250 μL 1× Passive lysis buffer (Promega) at room temperature for 15 minutes. The lysate was cleared by isolating cell debris by centrifugation and stored at −80°C unless used immediately for luminescence measurement. For luminometric measurement, 100 μL LARII buffer containing D-luciferin was dispensed in each well of the luminometer plate followed by 20 μL of cell lysate to measure *Firefly* luminescence. After measuring firefly luminescence, 100 μL Stop & Glo reagent containing quencher and substrate for *Renilla* luciferase was added to measure respective responsive luminescence. Data were normalized using individual well's *Renilla* luminescence. Each experiment was performed in triplicates and repeated three times.

Bioplex assay for chemokine and cytokine measurement

The concentration of 17 chemokines, cytokines, and growth factors in culture supernatants of control or R1881 treated LNCaP cells was determined using the Bioplex Pro Human Cytokine 17-plex assay system (Bio-Rad) according to manufacturer's protocol. Culture super-natant from vehicle and R1881 treated LNCaP, and LAPC4 cells were collected at 3- and 6-day timepoints, and stored at −80°C until further analysis. Data were collected on the Bio-Rad BioPlex 200 instrument and analyzed using the Bio-Plex Manager (Bio-Rad Laboratory).

Autophagosome flux measurement

Cells were plated on 60 mm dishes to obtain 80% confluence on the next day. Cells were transfected with tandem mRFP-GFP fluorescent-tagged LC3 (ptfLC3; Addgene #21074). A total of 24 hours post-transfection, cells were trypsinized and plated on sterile glass-bottom dishes at a 40%–50% confluency and treated with androgens. Autophagosomes are labeled as green and red dual-positive puncta and autolysosomes appear as red puncta as the green puncta is pH sensitive and quenched by the acidic lysosomal pH. Cells were then imaged using a live cell Zeiss LSM780-FCS Single-point, laser scanning confocal microscope. Images were processed using the ImageJ software. Cells with predominantly yellow RFP/GFP (autophagosome) or red RFP (autolysosome) puncta were counted and analyzed from at least 20 fields. Each experiment had images from at least five random fields and repeated three times.

Mouse xenografts and treatment

Using a Johns Hopkins Animal Care and Use Committee approved protocol, adult athymic nude mice were inoculated subcutaneously in the flank with the LNCaP human prostate cancer cell lines in 200 μL of Matrigel. Mice were divided into two groups, and the treatment group was implanted with two 1-cm-long silastic implants filled with testosterone as described previously (6). Tumors were harvested 2- and 4-day post-treatment and fixed in 10% buffered formalin and processed for IHC and hematoxylin and eosin staining. Natural killer (NK) cells were identified using antiCD57-PE (Santa Cruz Biotechnology) and antiCD49b-FITC (Santa Cruz Biotechnology) antibodies. F4/80-Alex-afluor 488 and Ly-6G-Alexafluor 488 antibodies (BioLegend) were used to stain the macrophages and neutrophils cells, respectively. Stained sections were imaged using Zeiss LSM 700 laser confocal microscope. Images were analyzed using the image processing package Fiji. NK cells, macrophages, and neutrophils were counted per field from at least five fields and plotted as mean values.

Patient materials

The study was conducted in accordance with ethical guidelines as outlined by the Declaration of Helsinki. The Institutional Review Board approved this study at Johns Hopkins, and all accrued patients provided written informed consent. Biopsies from metastatic lesions were obtained from patients with CRPC, under a prospective protocol (clinicaltrials.gov: NCT03554317) examining the use of SupraT as a treatment for metastatic CRPC. These patients had previously been treated with standard ADT as well as next-generation anti-androgen therapy using abiraterone and/or enzalutamide. Biopsies were typically obtained from soft-tissue metastatic sites (lymph nodes, liver, and lung) using an 18-gauge core biopsy needle and were collected before and 12 weeks after starting the SupraT treatment. For each metastatic biopsy, at least two fresh cores were collected for immediate flash freezing in liquid nitrogen (frozen tissue method), and at least two separate cores for formalin-fixed and paraffin-embedded sections (FFPE method). A dedicated tissue technician was called at the biopsy suite to initiate processing steps, including FFPE preparation within 30 minutes of biopsy collection. All samples were evaluated for adequacy and assessment of tumor-to-normal ratio by an expert urological pathologist. FFPE specimens were processed according to the standard procedures at the Johns Hopkins Pathology Department.

IHC staining and CD8 density measurement by image analysis

Chromogenic IHC for CD8 was performed as follows. Sections of 4-μm thickness were cut and placed on superfrost plus slides. Paraffin sections were baked on a hot plate at 60°C for 10 minutes, dewaxed using xylene, rehydrated in a series of graded alcohols to distilled water, and finally rinsed in distilled water with 0.1% Tween 20. Slides were transferred to a glass jar filled with a suitable antigen retrieval solution. The glass jar was irradiated in a microwave oven at full power for 1 minute, followed by 15 minutes at power level 20. Slides were cooled for 5 minutes at room temperature and washed 2× in tris-buffered saline with 0.1% Tween 20 (TBST). Tissues were subjected to endogenous peroxidase blocking using hydrogen peroxide for 5 minutes. Slides were then incubated with CD8 (DAKO, Clone: C8/144B) antibody for 45 minutes at room temperature, rinsed with TBST, and incubated with the secondary antibody (PowerVision Poly-HRP Anti-Mouse IgG, Leica, PV6119) for 30 minutes. Following incubation with the chromogen, 3-Amino-9-Ethylcarbazole (AEC) for 20 minutes, slides were counterstained with hematoxylin. After counterstaining, slides were washed with tap water for 2 minutes and distilled water for 1 minute and mounted using VectaMount AQ, Vector H-5501.

Whole biopsy slides stained for CD8 were scanned on a Roche-Ventana DP200 whole slide scanner and analyzed using the HALO 3.0 (Indica Labs) software. Regions of interest (ROI) consisted of tumor tissue that was delineated manually by a pathologist with expertise in prostate pathology. In cases with clear lymph node tissue from lymph node biopsies, regions were chosen to avoid encompassing the lymphoid tissue apart from the tumor. T cells were delineated using the cytonuclear IHC module in HALO. CD8 density was calculated as the number of T cells per mm^2 of ROI. Cell density measured using HALO were verified by manual counting in a subset of cases.
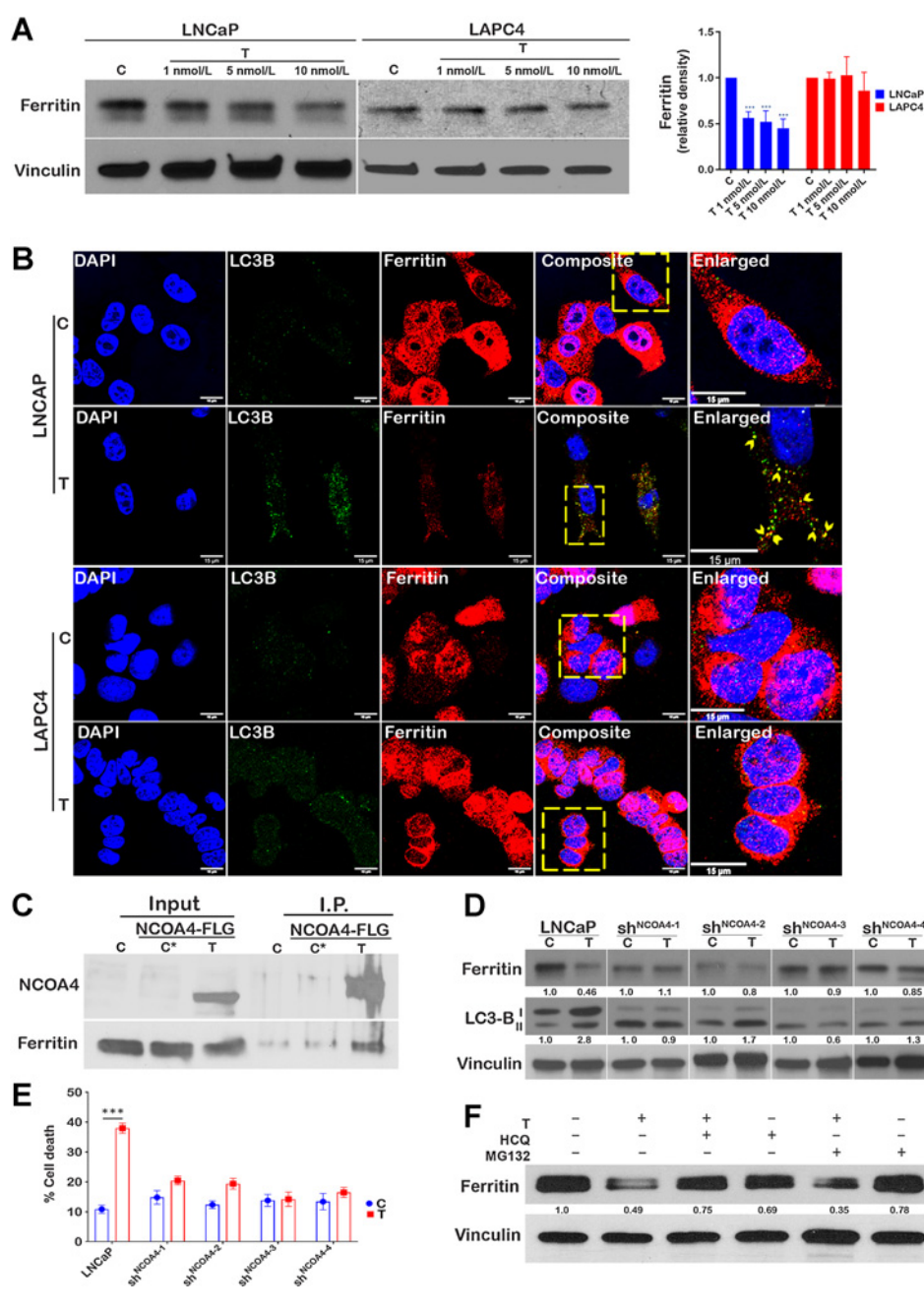
Statistical analysis

Suitable central tendency values were calculated for all the quantitatively measurable variables and were used for the analysis of statistical significance. Parametric analysis was performed to compare mean values after estimating the normal distribution unless otherwise specified. These analyses were performed using Prism version 6.0 (GraphPad Software), and a value of $P \leq 0.05$ was considered significant in all the statistical analyses.

Results

Our previous work demonstrated that sensitivity to SupraT differed among prostate cancer cell lines (6). Cell-cycle analysis revealed that SupraT causes a growth inhibitory accumulation of LNCaP cells in the G_0–G_1 phase, while LAPC4 cells show the opposite response and continue to proliferate (Supplementary Fig. S1A and S1B). Furthermore, the clonogenic analysis revealed that SupraT significantly decreases the clonogenic potential of SupraT-sensitive LNCaP cells (Supplementary Fig. S1C and S1D). To understand whether sensitivity to SupraT reflected DNA repair mutations in these cancer lines, we searched the COSMIC cell line database for mutations in DNA repair genes in prostate cancer lines (Supplementary Table S3). Strikingly, our analysis revealed that sensitivity to hormone exposure correlated directly with the number of DNA repair mutations harbored by the cell types (LNCaP > VCaP > LAPC4), mirroring our clinical data (6, 11). 22R-v1, another AR-positive line that is castration resistant (15) was not inhibited by SupraT (Supplementary Fig. S1E). We hypothesized that due to the prevalence of DNA repair mutations, LNCaP and VCaP cells (the intermediate sensitivity line) treated with SupraT might not repair DSBs induced by androgens and instead undergo a DNA repair

crisis, leading to apoptosis. However, contrary to our hypothesis, none of the prostate cancer cell lines treated with synthetic androgen R1881 had any substantial enhancement of PARP cleavage (Supplementary Fig. S2A). We also measured Annexin-V positivity, an early marker of apoptosis, in the highly sensitive LNCaP cells and found no significant increase in Annexin-V after treatment (Supplementary Fig. S2B). This suggested that the decrease in cell number upon testosterone treatment in the sensitive cell lines might likely also involve a nonapoptotic cell death mechanism. We, therefore, probed whether necrotic markers were induced upon SupraT treatment (Supplementary Fig. S2C), and found them to be markedly reduced or unchanged, ruling out necrotic induction by SupraT. Recently, ferroptosis, a nonapoptotic cell death mechanism, has been linked to autophagy (16, 17). We first determined whether SupraT can induce autophagy in prostate cancer lines. Treatment of prostate cancer cell lines demonstrated that the synthetic androgen, R1881, notably induces autophagy in the SupraT-sensitive LNCaP and VCaP cells, while basal autophagy in the SupraT-insensitive LAPC4 and 22Rv1 cells remained largely unaffected upon treatment (Supplementary Fig. S3A). We did not find global upregulation of key autophagy proteins such as Beclin or ATG12 (Supplementary Fig. S3B). However, we did find both the number of autophagosomes and autophagy flux (evaluated using an autophagy flux sensor) increased only in LNCaP cells as compared with LAPC4 cells upon treatment with androgens (Supplementary Fig. S3C). These results prompted us to determine whether SupraT is able to differentially induce ferroptosis in prostate cancer cells that are sensitive to androgen.

Ferroptosis involves iron-dependent accumulation of toxic lipid peroxides that leads to cell death (18). Degradation of the iron storage protein ferritin through a specialized form of autophagy, termed ferritinophagy, increases the labile pool of iron, leading to an increase in lipid peroxides (19). We sought to determine whether ferritinophagy is induced by SupraT. As depicted in **Fig. 1A**; Supplementary Fig. S4A, SupraT causes a dose-dependent decrease in ferritin levels in LNCaP and VCaP cells compared with LAPC4 and 22Rv1 cells, where ferritin levels remain unchanged. We confirmed whether decrease in ferritin level is indeed through testosterone by treating cells with DHT, a high-affinity testosterone metabolite. As shown in Supplementary Fig. S4B, supraphysiologic levels of DHT decreased ferritin levels in LNCaP cells but not in LAPC4 cells. Confocal images of SupraT-treated LNCaP cells revealed that ferritin colocalized with LC3B-positive autophagosomes (**Fig. 1B**). Because NCOA4 interacts with ferritin and mediates its autophagic degradation (19–21), we probed for NCOA4 and found that NCOA4 is induced by SupraT (Supplementary Fig. S4C), and interacts with ferritin in a SupraT-dependent manner (**Fig. 1C**). Furthermore, knockdown of NCOA4 in LNCaP cells (Supplementary Fig. S4D) inhibited R1881-induced ferritin degradation and decreased cell death. (**Fig. 1D** and **E**). Knockdown of NCOA4 also decreased SupraT-induced autophagy (**Fig. 1D**). To determine whether ferritin is indeed degraded through autophagy, we treated cells with hydroxychloroquine, an autophagy inhibitor, and MG-132, a proteasome inhibitor, and evaluated its effect on ferritin degradation upon SupraT treatment. As seen in **Fig. 1F**, hydroxychloroquine prevented the degradation of ferritin by SupraT, suggesting that ferritin is degraded through autophagy. We evaluated the functional consequence of decreased ferritin on lipid peroxide formation using the lipid peroxide sensor, C11-BODIPY (18, 22), which fluoresces green upon oxidation. As shown in **Fig. 2A** and **B**, R1881-treated LNCaP cells but not LAPC4 had increased lipid peroxides and labile iron pool (**Fig. 2C**) compared with vehicle-treated controls. Next, we investigated whether SupraT induces pro-ferroptotic gene

Figure 1.
SupraT induces ferritinophagy in prostate cancer cells. **A,** Western blot analysis showing ferritin and loading control vinculin in LNCaP and LAPC4 cells treated with indicated concentrations (nmol/L) of R1881 (T) and vehicle (C) for 72 hours. A representative of three independent experiments. Ferritin, ~21 kDa; loading control vinculin, 124 kDa. Bar graph shows mean relative density from three experiments. **B,** A representative single confocal section from three independent experiments is shown. Each experiment had at least five random fields. LNCaP and LAPC4 cells were stained for LC3B (green) and ferritin (red). Rightmost panels show enlarged inset images of a region of interest, and the arrowhead indicates colocalization of ferritin in autophagosomes (LC3B). **C,** Western blot analysis for immunoprecipitated NCOA4-FLAG for interaction with ferritin in LNCaP cells transfected with human NCOA4α–pHAGE-C-FLAG-HA plasmid. Nontransfected (C) and NCOA4α–pHAGE-C-FLAG-HA–transfected vehicle-treated cells (C*) were used as controls. A representative of three independent experiments. NCOA4, 70 kDa; ferritin, ~21 kDa. **D,** Ferritin and LC3B levels probed by Western blot analysis in vehicle (C)- or R1881 (T)-treated LNCaP or NCOA4 shRNA lentiviral particle–transduced LNCaP sh^{NCOA4} (1–4) cells. A representative of three independent experiments. Ferritin, ~21 kDa; LC3-B, 14,16 kDa; loading control vinculin, 124 kDa. **E,** Cell death in LNCaP and LNCaPshNCOA4 (1–4) measured using trypan blue exclusion assay, control (C), 10 nmol/L R1881 (T). Bar graph shows mean percent of cell death from three independent experiments and error bar shows SD. **F,** Western blot analysis for ferritin LNCaP cells treated with vehicle, 10 nmol/L R1881 (T), 10 μmol/L hydroxychloroquine (HCQ), 10 μmol/L MG132 (MG132) alone or combination of T with either of HCQ or MG132. A representative of three independent experiments. Ferritin, ~21 kDa; loading control vinculin, 124 kDa. Scale bars, 15 μm (**B**). ***, $P < 0.001$.

expression (16, 23). Pro-ferroptotic genes such as *ALOX5*, *PTGS2*, and *NCOA4* were increased many folds over vehicle controls (**Fig. 2D**). We further confirmed that SupraT-induced cell death in LNCaP is indeed through ferroptosis, as treatment with a combination of R1881 and a ferroptosis inhibitor, ferrostatin-1, abrogated cell death (**Fig. 2E** and **F**). A similar abrogation of SupraT-induced cell death was observed in VCaP cells, which demonstrates intermediate sensitivity to SupraT (Supplementary Fig. S4E). Moreover, treatment of LNCaP and LAPC4 cells with DHT or a combination of DHT and ferrostatin-1 had the same effect (Supplementary Fig. S4F).

To investigate whether there is a direct link between response to SupraT, autophagy, and DNA repair, we treated SupraT-sensitive LNCaP cells, which harbor several DNA repair gene mutations (Supplementary Table S3), with R1881 and stained cells for autophagosomes and DSBs. We postulated that cells harboring damaged DNA would have increased autophagy in response to DNA damage stress. Interestingly, LNCaP cells with increased autophagosomes displayed a smaller number of γH2AX puncta (Pearson correlation = −0.78; **Fig. 3A** and **B**). This suggested that cells undergoing autophagy in response to SupraT might clear their damaged DNA more efficiently. Autophagy, being a dynamic event, renders visualization of fractions of autophagosomes carrying damaged DNA a challenge. Hydroxychloroquine prevents the fusion of autophagosomes to lysosomes, leading to accumulation of autophagosomes (24). Treatment of

Figure 2.
SupraT induces ferroptosis in prostate cancer cells. **A,** Representative fluorescence microscopy images of control (C) and 10 nmol/L R1881-treated (T) LNCaP and LAPC4 cells from three independent experiments showing C11-BODIPY staining for oxidized membrane lipid (green fluorescence). Each experiment had at least five random field images. Enlarged inset images in the rightmost panels show a region of interest. **B,** Bar graph showing fold change in levels of control normalized oxidized lipids (Bodipy C11) in LNCaP and LAPC4 cells, measured by image analysis using ImageJ. **C,** Measurement of labile iron pool (Fe2$^+$) in LNCaP and LAPC4 cells. Bar graph shows fold change in labile iron pool calculated by normalizing to untreated control cells. **D,** Quantitative RT-PCR analysis for a panel of pro-ferroptotic genes in 10 nmol/L R1881-treated LNCaP and LAPC4 cells after 72 hours. Vehicle control was used for normalization to calculate the fold change. A representative of three independent experiments. Bar graph indicates fold change upon SupraT treatment. **E,** Cell death measured using trypan blue exclusion assay. Control (C), 10 nmol/L R1881 (T), 10 μmol/L ferrostatin (F), or combination (T+F) shown as mean from three measurements, with error bar showing SD. **F,** Bar graph showing the mean of the number of colonies from three independent measurements counted using Fiji software for treatment conditions stated in **E**, with error bars showing SD. Asterisk (*) compares T or F versus C and # indicates comparison between T and T+F. Both * and # indicate statistically significant differences ($P < 0.05$). Scale bars, 100 μm (**A**). *, $P < 0.05$; **, $P < 0.01$; ***, $P < 0.001$; ###, $P < 0.001$.
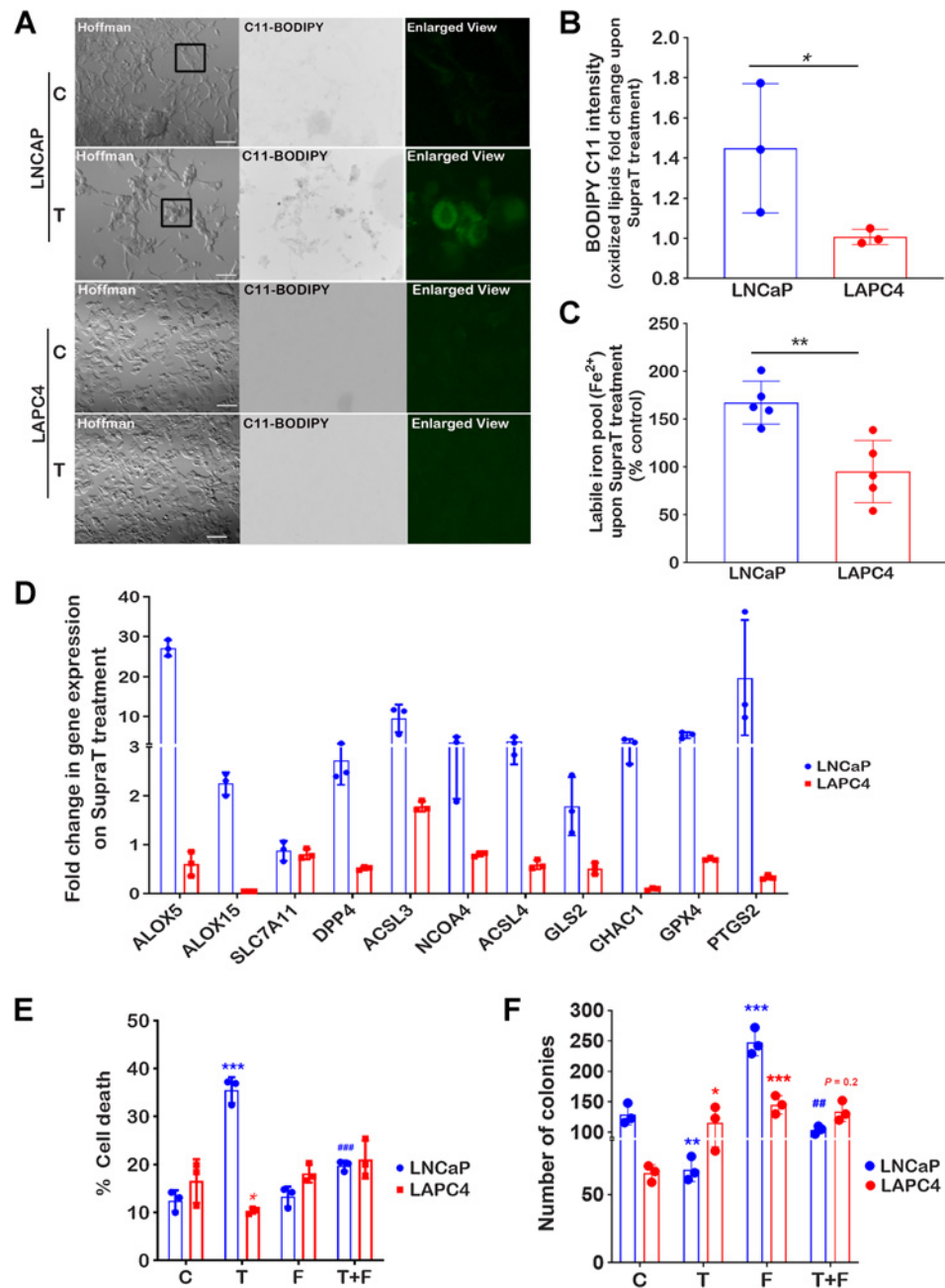
prostate cancer cell lines with a combination of hydroxychloroquine and R1881 revealed marked localization of cytoplasmic DNA in LNCaP cells compared with the fewer cytoplasmic DNA puncta displayed in VCaP cells, which have intermediate DNA repair gene mutations (Supplementary Table S3). The SupraT-insensitive LAPC4 cells, however, did not show any cytoplasmic DNA (**Fig. 3C**). Intriguingly, although we did find induction of DSBs in SupraT-treated LNCaP NCOA4 knockdown cells, similar to wild-type cells (Supplementary Fig. S5A), we did not find any cytoplasmic DNA (Supplementary Fig. S5B) in these cells after SupraT treatment. This could be as a result of abrogation of autophagy induction as evident from the number of autophagosomes between control and SupraT-treated cells (Supplementary Fig. S5C). To ensure that the observed cytoplasmic

DNA was not mitochondrial DNA, we stained cells with antibodies against mitochondrial complex IV subunit I and LC3B. We did not find any notable colocalization of mitochondria with autophagosomes (**Fig. 3D**). However, we did find marked colocalization of cytoplasmic DAPI staining with LC3B in SupraT-treated cells, indicating that the cytoplasmic DNA is present in autophagosomes (**Fig. 3E**). DAPI intensity peaked in the lumen of autophagosomes, indicating that the DNA was indeed present within the autophagosomes (**Fig. 3F**). To ascertain whether the DNA within the autophagosomes harbored damaged DNA, we stained cells treated with a combination of hydroxychloroquine and SupraT with γH2AX and LC3B. As seen in **Fig. 3G**, LC3B and γH2AX colocalize with DAPI signals in the cytoplasm. This suggests that SupraT-induced damaged DNA can be shuttled to the
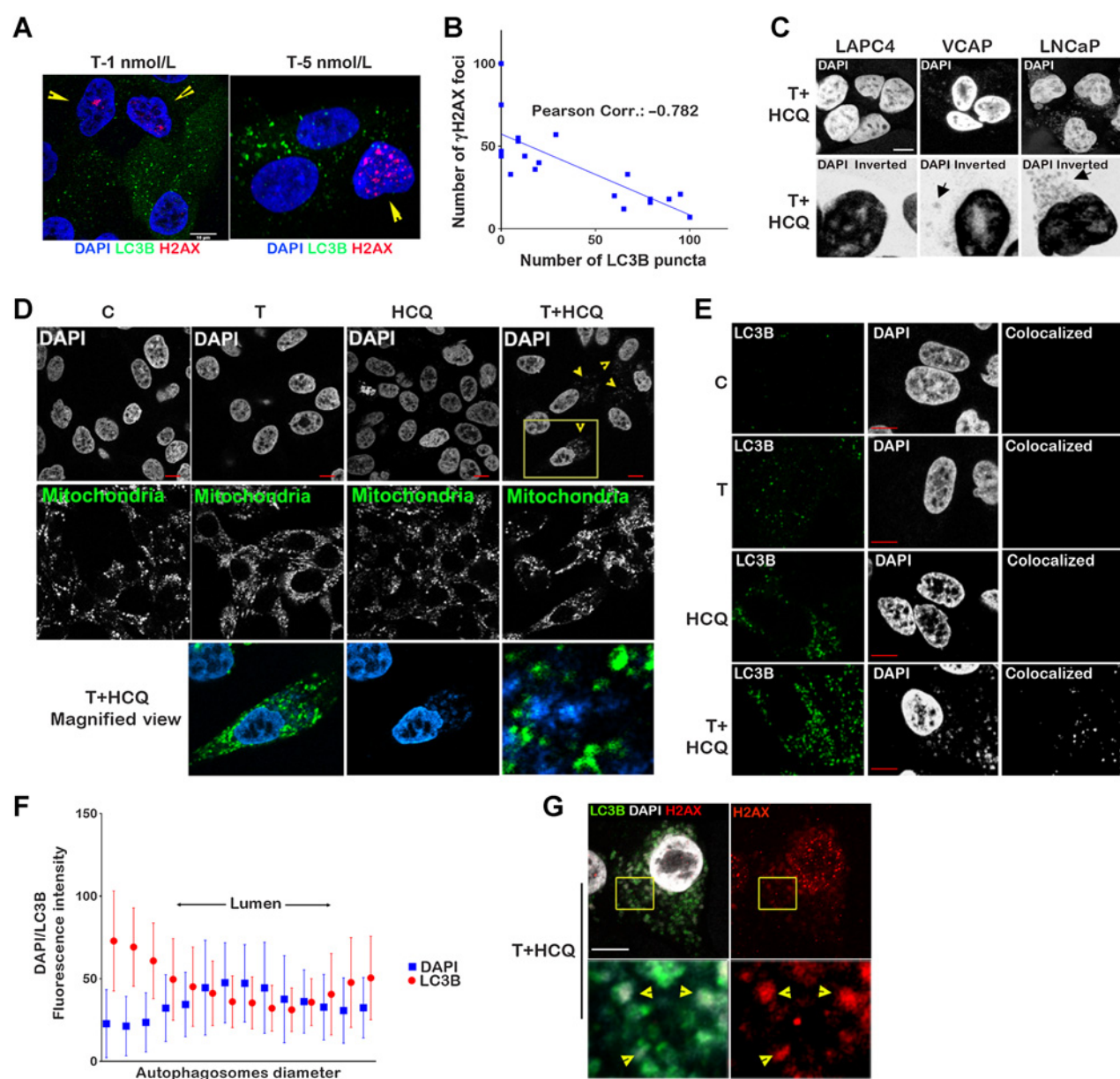
Figure 3.
SupraT induces nucleophagic degradation of unrepaired damaged DNA. **A,** A representative single confocal section is shown from three independent experiments. LNCaP cells stained for γH2AX (red) and LC3B (green) after treatment with 1 and 5 nmol/L R1881. Arrowheads indicate cells harboring γH2AX foci with lower LC3B puncta. Each experiment had at least five random field images. **B,** Scatter plot showing a correlation between the number of LC3B puncta and the number of γH2AX foci counted ($n = 19$ measurements). Counting of puncta was performed using the image analysis software Fiji. **C,** Confocal microscopy images for prostate cancer cell lines treated with 10 nmol/L R1881 (T) and hydroxychloroquine (HCQ). Each experiment had at least five random field images. The bottom panel is an inverted and magnified image of a single cell in the view-field for better visualization. Arrows, localization of cytoplasmic DNA. **D,** Confocal images showing mitochondrial staining in LNCaP cells treated with vehicle (C), 10 nmol/L R1881 (T), 10 μmol/L HCQ, or combination of T+HCQ for 72 hours. Bottom panel shows a magnified view for enhanced visualization. Each experiment had at least five random field images. **E,** Photomicrographs showing colocalization of LC3B (green) and DAPI (gray) in LNCaP cells treated with control (C), 10 nmol/L R1881 (T), HCQ (10 μmol/L) or T+HCQ treated LNCaP cells (72 hours). Rightmost panel shows colocalized pixels. **F,** Graphical representation of fluorescence intensities of LC3B and DAPI on individual autophagosomes ($n = 16$ measurements). **G,** Photomicrographs showing LC3B (green) and γH2AX (red) in LNCaP cells after 72 hours of treatment with T+HCQ. Bottom panels show the enlarged insets with a region of interest. Arrowheads in the bottom left image indicate the presence of DNA (DAPI) in autophagosomes (LC3B), and bottom right image shows γH2AX positivity in DNA present in those autophagosomes. Each experiment had at least five random field images. Scale bars, 5 μm (**A**), 10 μm (**C**), 10 μm (**D**), 10 μm (**E**), and 10 μm (**G**).

cytoplasm for autophagosome-mediated degradation. This implies that SupraT might induce two parallel autophagy-mediated phenomena, ferritinophagy and nucleophagy, both of which may be responsible for the growth inhibitory effects of SupraT.

Cytosolic DNA is seen as a stimulant by the innate immune system as it is detected by DNA sensors in the cytoplasm that activate the adaptor protein STING and downstream innate immune signaling (25, 26). The STING promoter harbors an AR binding motif (Supplementary Fig. S6A); however, we did not find any induction of the STING transcript or STING promoter by treatment with SupraT (Supplementary Fig. S6B and S6C). Intriguingly, treatment with SupraT induced the STING protein as well as the RNA sensors RIG-I and MDA5 proteins in the SupraT-sensitive LNCaP cells (Fig. 4A). Upon activation, monomeric STING dimerizes and translocates from the ER to autophagosome-like vesicles (27, 28). Separa-

tion of cellular homogenates on sucrose gradients revealed STING cofractionates with LC3B-positive autophagosomes in SupraT-treated cells (Fig. 4B). To confirm that STING is indeed activated upon SupraT treatment, we performed a STING dimerization assay, a gold standard for STING activation (26). As shown in Fig. 4C, treatment with SupraT activates STING in LNCaP compared with LAPC4 cells. Interestingly, SupraT also activated MAVS oligomerization, indicating that the RNA sensing pathway was activated as well (Fig. 4D). Mislocalized and damaged DNA can also be detected by AIM2 (29). The AIM2 promoter harbors an AR binding motif (Supplementary Fig. S6D); hence we first measured AIM2 transcript and protein levels. We did not find any induction of AIM2 promoter activity, AIM2 transcript levels or protein by SupraT (Supplementary Fig. S6E and S6F; Fig. 4E). Neither did we find SupraT-mediated activation of downstream inflammasomes, as evaluated by IL1β cleavage, ruling out
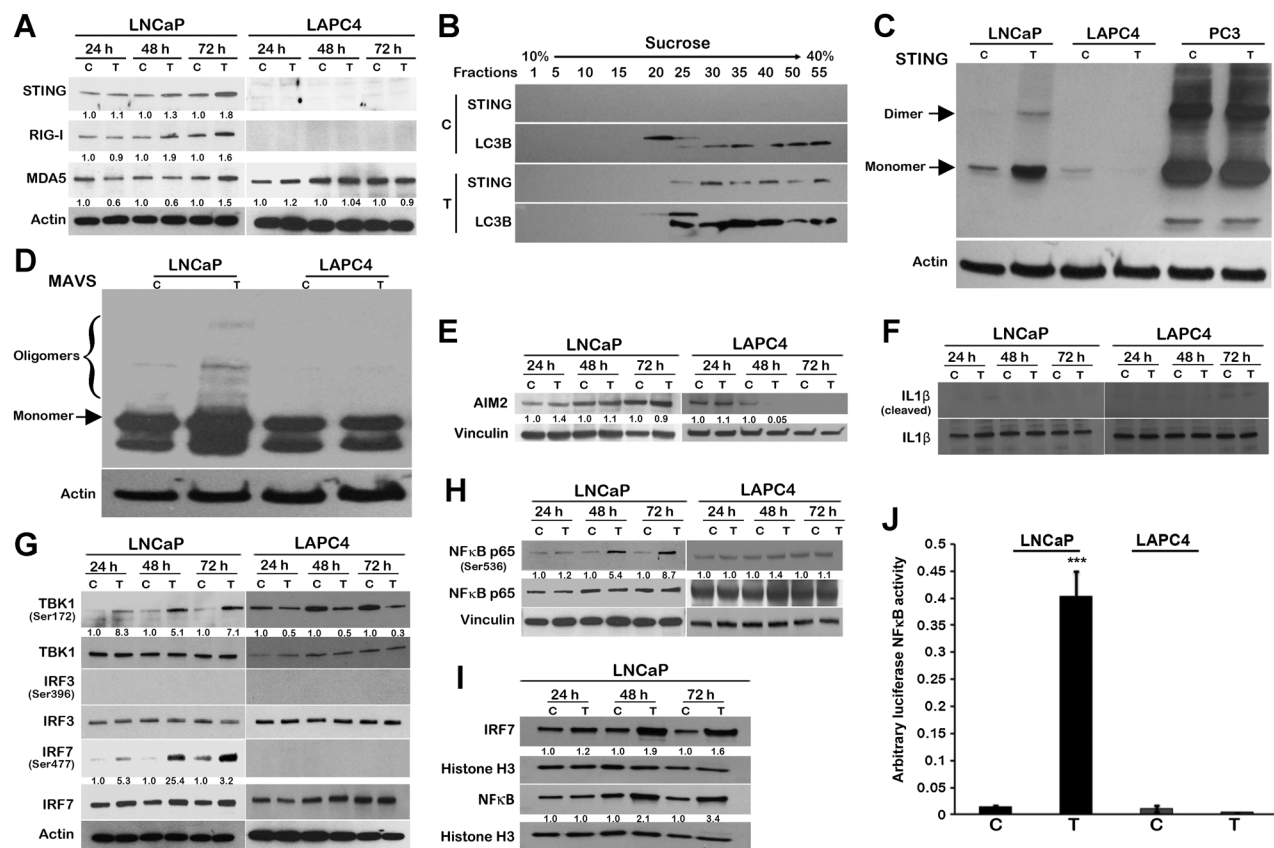

Figure 4.
SupraT activates cytoplasmic nucleic acid sensors and subsequent NFκB signaling. **A,** Western blot analysis showing DNA (STING)- and RNA (RIG-I and MDA5)-specific sensors along with actin as a loading control in LNCaP and LAPC4 cells treated with vehicle control (C) or 10 nmol/L R1881 (T) in a time-dependent manner. A representative of three independent experiments. STING, 33–35 kDa; RIG-I, 102 kDa; MDA5, 135 kDa; loading control actin, 43 kDa. **B,** Immunoblotting for LC3B and STING on fractions isolated using sucrose gradient centrifugation from LNCaP cell homogenates after 72 hours of 10 nmol/L R1881 treatment with 10 nmol/L R1881 (T) or vehicle control (C). A representative of at least three independent experiments. STING, 33–35 kDa; LC3B, 14, 16 kDa. **C** and **D,** Native Western blot probing for STING (**C**) and MAVS (**D**) in prostate cancer cell lines treated with vehicle (C) or 10 nmol/L R1881 (T). A representative of three independent experiments; loading control actin, 43 kDa. PC3 cells with constitutive expression of active STING were used as a positive control (**C**). **E** and **F,** Western blot analysis for AIM2 induction (AIM2; **E**) and signaling (IL1β; **F**) in prostate cancer cell lines treated with vehicle (C) or 10 nmol/L R1881 (T) in a time-dependent manner. A representative of three independent experiments. AIM2, 40 kDa; IL1β, 17,31 kDa; cleaved IL1β, 17 kDa; loading control vinculin, 124 kDa. Immunoblotting for IFN regulatory genes IRF7, IRF3, TBK1 (**G**), and NFκB (**H**) in prostate cancer cell lines treated with vehicle (C) or10 nmol/L R1881 (T) at 24, 48, and 72 hours. Activated forms of all IFN regulatory genes were probed by respective phosphorylation-specific antibodies. A representative of at least two independent experiments. Phospho-TBK1, 84 kDa; TBK1, 84 kDa; Phospho IRF3, 45–55 kDa; IRF3, 50–55 kDa; Phospho-IRF7, 65 kDa; IRF7, 65 kDa; loading control actin, 43 kDa. **I,** Nuclear localization of IRF7 and NFκB in LNCaP cells after treatment with vehicle (C) or 10 nmol/L R1881 (T) at indicated timepoints. A representative of at least two independent experiments. IRF7, 65 kDa; NFκB, 65 kDa; loading control histone H3, 17 kDa. **J,** Bar graphs showing mean of luciferase NFκB activity in LNCaP cells after treatment with vehicle (C) or 10 nmol/L R1881 (T) using luciferase-based NFκB reporter assay from three independent measurements and error bars show SD. Asterisks indicate statistically significant differences (P < 0.05). ***, P < 0.001.

the involvement of AIM2-mediated inflammasome signaling by SupraT (**Fig. 4F**). We found a similar activation of STING, albeit less robustly, in VCaP cells (Supplementary Fig. S7A). Interestingly in VCaP cells, STING appeared as a tetramer as reported for STING activation in some studies (30). We did not find any activation of STING in the SupraT-insensitive 22Rv1 cells (Supplementary Fig. S7A), neither did we find any activation of MAVS in both VCaP and 22Rv1 cells (Supplementary Fig. S7C). We next investigated whether the observed effect is indeed due to testosterone by treating cells with DHT. In agreement with our findings using R1881, we found DHT robustly increased autophagy in LNCaP cells but not in LAPC4 cells (Supplementary Fig. S4B). DHT also activated STING and MAVS preferentially in LNCaP cells (Supplementary Fig. S7B and S7D); however, the activation was not as robust as R1881. This may be due to the fact that persistent H2AX foci are not observed in DHT-treated cells as compared with R1881 (9), as DHT is rapidly metabolized (31, 32).

Following its own activation, STING activates the Tank binding kinase 1 (TBK1), which in turn phosphorylates and activates IFN regulatory factors (IRF), including IRF3, IRF7, and NFκB, leading to the induction of immune response genes (25). Although we did not find any activation of IRF3 by SupraT treatment (**Fig. 4G**; Supplementary Fig. S7E), our data indicate that TBK1, IRF7, and NFκB canonical p65 subunit were activated upon SupraT treatment in LNCaP and VCaP cells (**Fig. 4G** and **H**; Supplementary Fig. S7F). Activated p65 and IRF7 increased in the nucleus (**Fig. 4I**). Similar to LAPC4 cells, 22Rv1 cells did not show an induction of NFκB or IRF7 signaling (Supplementary Fig. S7F). We performed an NFκB promoter-reporter assay, which confirmed the functional activation of NFκB in SupraT-sensitive cells (**Fig. 4J**). Intriguingly, we found SupraT stabilized NFκB inducing kinase (NIK), a kinase central to the noncanonical NFκB pathway (**Fig. 5A**). NIK phosphorylates the noncanonical p100 subunit of NFκB and marks it for processing by a proteasome into the smaller p52 subunit, which subsequently dimerizes with RELB to activate transcription of target genes. Treatment with SupraT led to the formation of p52 and induction of RELB in the SupraT-sensitive LNCaP cells but not in VCaP cells (**Fig. 5A** and Supplementary Fig. S7F); probably reflecting differences in SupraT sensitivity of these cells. Immunofluorescence confirmed the nuclear translocation of p52 upon SupraT treatment (**Fig. 5B**). Furthermore, in line with nucleic acid sensor activation, treatment with DHT led to stabilization of RELB and NIK and phosphorylation of the canonical and noncanonical NFκB subunits downstream of nucleic acid sensors (Supplementary Fig. S7G). These data indicate that SupraT-induced DNA damage activates nucleic acid sensors and downstream NFκB signaling.

To find out whether NFκB responsive innate immune genes were activated by the nucleic acid sensors, we measured transcript levels of innate immune genes and found many genes were significantly upregulated in the SupraT-sensitive LNCaP and VCaP cell lines (**Fig. 5C**; Supplementary Fig. S7H). *CXCL10*, a chemokine, was increased (33) several folds in treated LNCaP cells both at transcript and protein level (**Fig. 5D** and **E**). *CXCL10* was also induced (less robustly) in VCaP cells but not in SupraT-insensitive 22Rv1 cells (Supplementary Fig. S7I). Furthermore, DHT was able to induce CXCL10 (less robustly than R1881) preferentially in LNCaP cells as compared with LAPC4 cells (Supplementary Fig. S7J). Bioplex assays confirmed the induction and secretion of CXCL10 and other chemokines upon SupraT treatment (Supplementary Table S4). To determine whether STING or RIG-I sensors play a role in the activation of downstream innate immune signaling, we created knockouts for

STING, RIG-I, and STING/RIG-I double knockouts (Supplementary Fig. S8A and S8B) and tested whether they abrogate CXCL10 induction. Knockout of STING did not abrogate *CXCL10* induction, but double knockouts and knockout of RIG-I alone decreased *CXCL10* expression (**Fig. 5F**). This suggested that both the nucleic acid sensors are activated in SupraT-sensitive cells and that RIG-I may play an essential role in amplifying the signal. RIG-I can also be activated by the expression of endogenous retroviruses (34). Our analysis revealed that some of the endogenous retroviruses harbor androgen response elements (Supplementary Fig. S8C). However, none of the endogenous retroviral transcripts investigated were upregulated by SupraT (**Fig. 5G**), suggesting activation of RIG-I may be primarily through cytoplasmic DNA, as indicated by others (35).

To tease out whether the canonical or the noncanonical NFκB pathway is important for innate immune gene signaling by SupraT, we made knockouts of TBK1 and other key components of the NFκB pathway (Supplementary Fig. S8D–S8F). Knockouts of p65, TBK1, and RELB each abrogated downstream *CXCL10* induction by SupraT without altering the growth inhibitory effect of SupraT on of these cells (**Fig. 5H**; Supplementary Fig. S8G). Induction or proteolytic processing of noncanonical subunits RELB and p100, respectively, by SupraT was totally abrogated in p65 and TBK1 knockouts (**Fig. 6A**), indicating that the canonical pathway is important for the activation of the noncanonical pathway and TBK1 may play a critical role in linking the two. Furthermore, knockouts of p65, RELB, and TBK1 each abrogated NIK stabilization compared with parental cells, knockouts of STING and RIG-I decreased NIK stabilization, and STING/RIG-I double knockouts totally diminished the NIK stabilization, mirroring that of the p65 and TBK1 knockouts (**Fig. 6B**). Intriguingly, knockouts of STING did not revoke induction or processing of p100, but knockouts of RIG-I alone decreased p100 induction. Furthermore, STING/RIG-I double knockouts had lower induction of RELB and p100 processing as compared with STING knockouts (**Fig. 6C**). While these data corroborate the involvement of both the nucleic acid sensors, STING and RIG-I may have opposite effects on the noncanonical NFκB signaling induced by SupraT-STING being suppressive and RIG-I being supportive.

To identify immune genes activated by SupraT and discern those regulated by the STING-TBK1-NFκB axis, we performed a Nanostring PanCancer IO 360 Gene Expression analysis using a panel of 770 unique immune-gene signatures. Of 57, differentially (>2.5 fold) expressed genes, 38% of immune genes were induced in a STING-TBK1-NFκB–dependent manner (**Fig. 6D**). We validated a panel of chemokines and cytokines that play a role in attracting immune cells using quantitative PCR, and in concurrence with our NanoString data, these genes were altered in a STING-TBK1-NFκB–dependent manner (**Fig. 6E**). The gene expression data further indicate that both innate and adaptive immune cells might home to and get activated by SupraT-induced cytokines and chemokines. To investigate whether SupraT is able to induce migration of NK cells, we conducted a transwell migration assay with human NK-92 cells and found the SupraT-sensitive cell line significantly increased migration of NK-92 cells upon treatment (**Fig. 6F**). We next established LNCaP xenografts in athymic nude mice, which exhibit robust NK-cell activation and harbor neutrophils and macrophages (36). In concordance with *in vitro* findings, SupraT led to an increase in autophagosomes, the presence of cytoplasmic DNA, and an increase in CXCL10 expression by tumor cells (**Fig. 7A** and **B**). The presence of autophagosomal DNA without any autophagy inhibition indicated that the dynamics of autophagosomal degradation differed *in vitro* and *in vivo* (**Fig. 7C**).
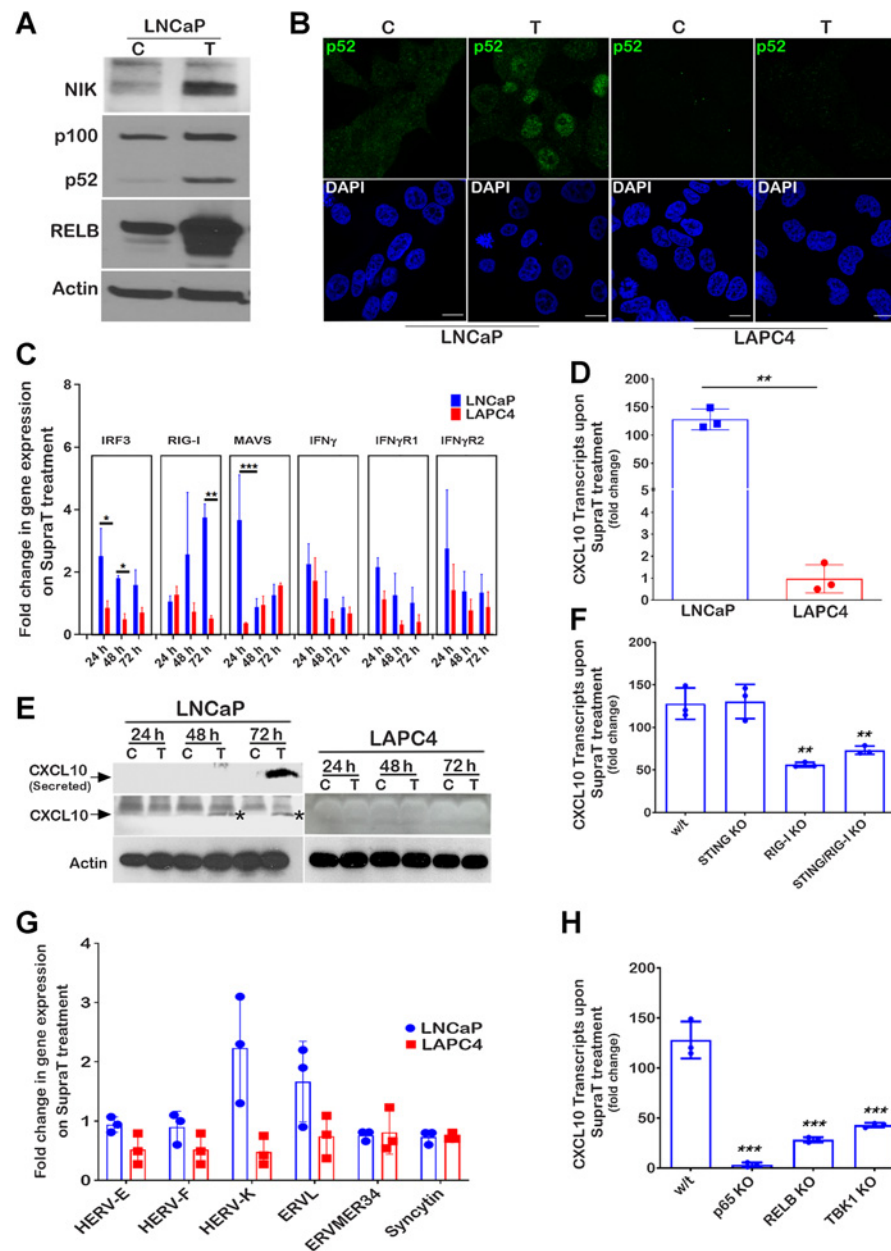
Figure 5.
SupraT-induced NFκB signaling drives innate immune response. **A,** Immunoblotting for NIK, p100, p52, and RELB proteins in vehicle control (C)– or 10 nmol/L R1881-treated (T) LNCaP cells. A representative of at least three independent experiments. NIK, 125 kDa; NFκB2 p100 and p52 120 and 52 kDa, respectively; RELB, 70 kDa; loading control actin, 43 kDa. **B,** Immunofluorescence images for the LNCaP and LAPC4 cells treated with vehicle (C) or 10 nmol/L R1881 (T) and stained with p52 (green) and DAPI (blue) for visualization of nuclear p52 protein. A representative of at least two independent experiments. Each experiment had at least five random field images. **C,** Quantitative RT-PCR for the IFN-related genes in 10 nmol/L R1881-treated LNCaP and LAPC4 cells for 24, 48, and 72 hours timepoints. Mean fold change data between LNCaP and LAPC4 cells were compared statistically, and an asterisk indicates a statistically significant difference ($n = 3$). Bar graph indicates fold change upon SupraT treatment. **D,** *CXCL10* transcript analysis using quantitative RT-PCR from total RNA isolated from vehicle- or 10 nmol/L R1881-treated LNCaP and LAPC4 cells ($n = 3$). Bar graph indicates fold change upon SupraT treatment. **E,** Western blot analysis for CXCL10 protein (lysates for cellular and culture media for secreted) for vehicle (C)- and 10 nmol/L R1881 (T)-treated LNCaP and LAPC4 cells made after 24, 48, or 72 hours post-treatment (band marked with asterisk*). A representative of at least two independent experiments. CXCL10, 10 kDa; loading control actin, 43 kDa. **F,** RT-PCR–based measurement for *CXCL10* transcripts in LNCaP or knockouts of RIG-I, STING, or both after treatment with 10 nmol/L R1881 for 72 hours. Bar graph indicates mean fold change upon SupraT treatment ($n = 3$) and an asterisk indicates a statistically significant difference ($P < 0.05$). **G,** Histogram showing endogenous retroviral transcripts in 10 nmol/L R1881-treated LNCaP or LAPC4 cells. Bar indicates a mean fold change upon SupraT treatment ($n = 3$), and the error bar indicates the SD from three replicate values. **H,** Expression of *CXCL10* transcripts in wild-type, p65 KO, RELB KO, and TBK1 KO LNCaP cells treated with 10 nmol/L R1881. Statistical significance is calculated between the wild-type and knockout variants of LNCaP cells. Bar graph indicates fold change upon SupraT treatment ($n = 3$) and an asterisk indicates a statistically significant difference ($P < 0.05$). Scale bars, 15 μm (**B**). *, $P < 0.05$; **, $P < 0.01$; ***, $P < 0.001$.
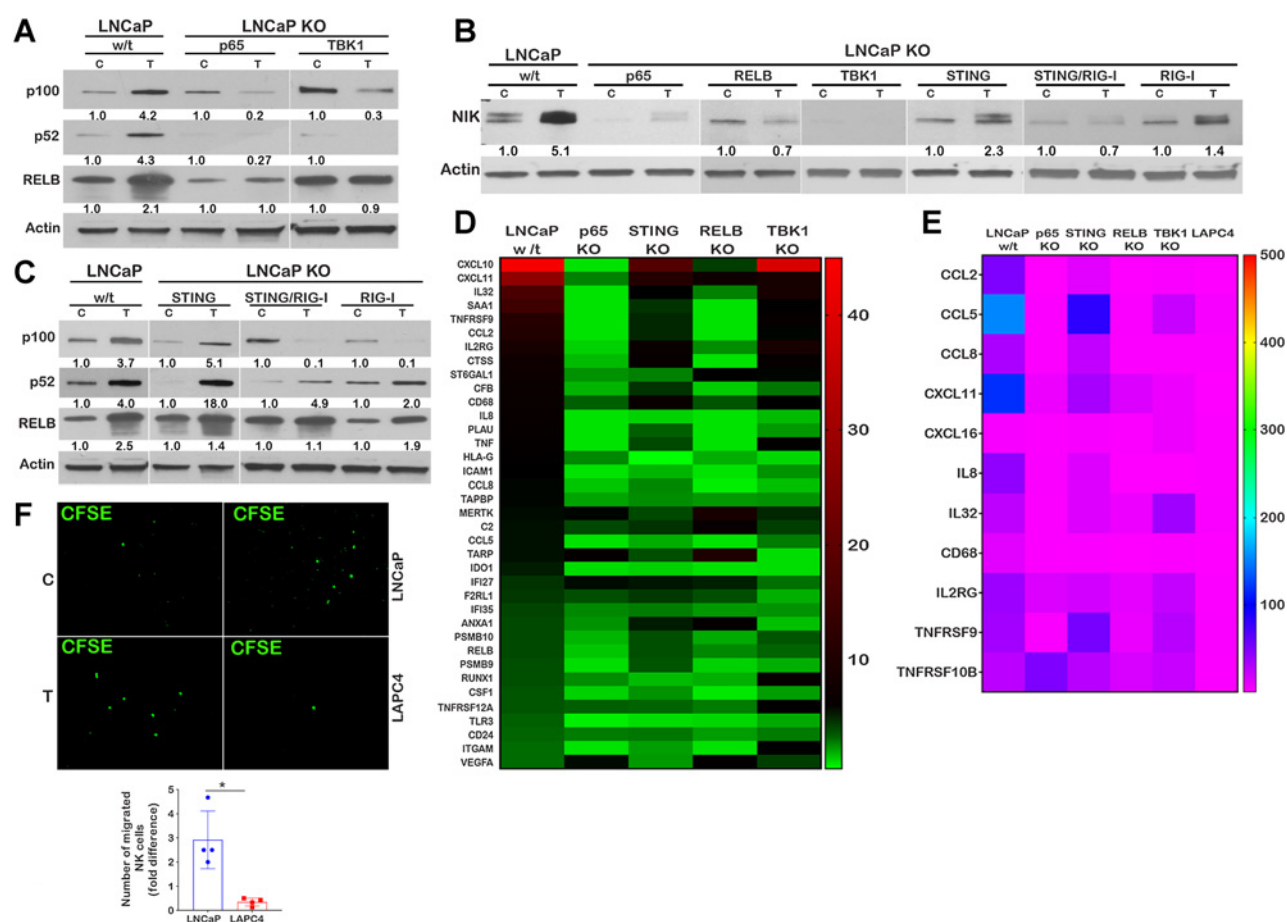
Figure 6.
SupraT activates both canonical and noncanonical NFκB signaling. **A,** Immunoblotting for p100, p52, and RELB protein to show noncanonical NFκB signaling in wild-type and knockout LNCaP cells treated with vehicle (C) or 10 nmol/L R1881 (T). A representative of three independent experiments. p100 and p52 120 and 52 kDa, respectively; RELB, 70 kDa; loading control actin, 43 kDa. **B,** Blot depicting stabilization of NIK in wild-type and all knockout cells treated with vehicle (C) or 10 nmol/L R1881 (T). A representative of three independent experiments. NIK, 125 kDa; loading control actin, 43 kDa. **C,** Levels of p100 and p52 protein in DNA and RNA sensors (RIG-I and STING) single and double knockouts in LNCaP cells treated with vehicle (C) or 10 nmol/L R1881 (T). A representative of three independent experiments. NF-κB2 p100 and p52 120 and 52 kDa, respectively; RELB, 70 kDa; loading control actin, 43 kDa. **D,** Heatmap depicting fold change for expression of a number of genes selected from pan-cancer immune profiling panel. Total RNA extracted from indicated samples was analyzed for 770 immune-related human genes using nCounter human PanCancer Immune Profiling Panel (NanoString). **E,** Heatmap showing relative expression levels of genes selected from the list of 57 genes that showed higher expression in NanoString analysis. Total RNA was analyzed using qRT-PCR, and data are shown as heatmap from a representative experiment of three independent experiments. **F,** Representative photomicrographs depict CFSE-labeled NK-92 cells migrated toward either vehicle (C)- or 10 nmol/L R1881 (T)-treated LNCaP or LAPC4 cells through 5 μmol/L Boyden chamber. Vehicle control normalized count of NK-92 cells plotted as a mean of four independent experiments on histograms, with error bars showing SD. Each experiment had at least five random field images. An asterisk indicates a statistically significant difference (P < 0.05). Scale bars, 100 μm (**F**). *, P < 0.05.

Staining for NK-cell markers CD57 and CD49b revealed a 17-fold induction in NK-cell migration to the tumor bed (**Fig. 7D**; Supplementary Fig. S9). A similar result was obtained when tumors were stained for macrophages and neutrophils (**Fig. 7E** and **F**). Prostate tumors are considered immunologically cold tumors with limited cytotoxic T-cell infiltration (37). The clinical significance of our data was investigated using biopsy from patients undergoing BAT therapy. As seen in **Fig. 7G**, BAT administration significantly increased the infiltration of CD8 T cells. In summary, these results indicate that SupraT may be able to activate immune cells through the NFκB pathway by activating nucleic acid sensors, especially in cells with defects in DNA repair pathways. Our data also indicate that SupraT may induce ferroptosis, a potentially immunogenic cell death mechanism.

Discussion

Strategies to overcome resistance to ADT can make a significant impact on the current outcomes of therapy. Several complementary mechanisms for the paradoxical effect of SupraT on prostate cancer have been described, including cellular senescence and cell death (38–41). Understanding how BAT works at the molecular and cellular levels might help in rationally combining BAT with other agents to achieve increased efficacy and tumor response. Our findings that the administration of SupraT may lead to ferroptosis mediated by lipid peroxides is intriguing. It is speculated that prostate cancer cells rely on lipid metabolism for their growth, and targeting lipid metabolism to overcome prostate cancer growth is viewed as a possible therapeutic strategy (42). SupraT may also influence both lipid uptake and synthesis,
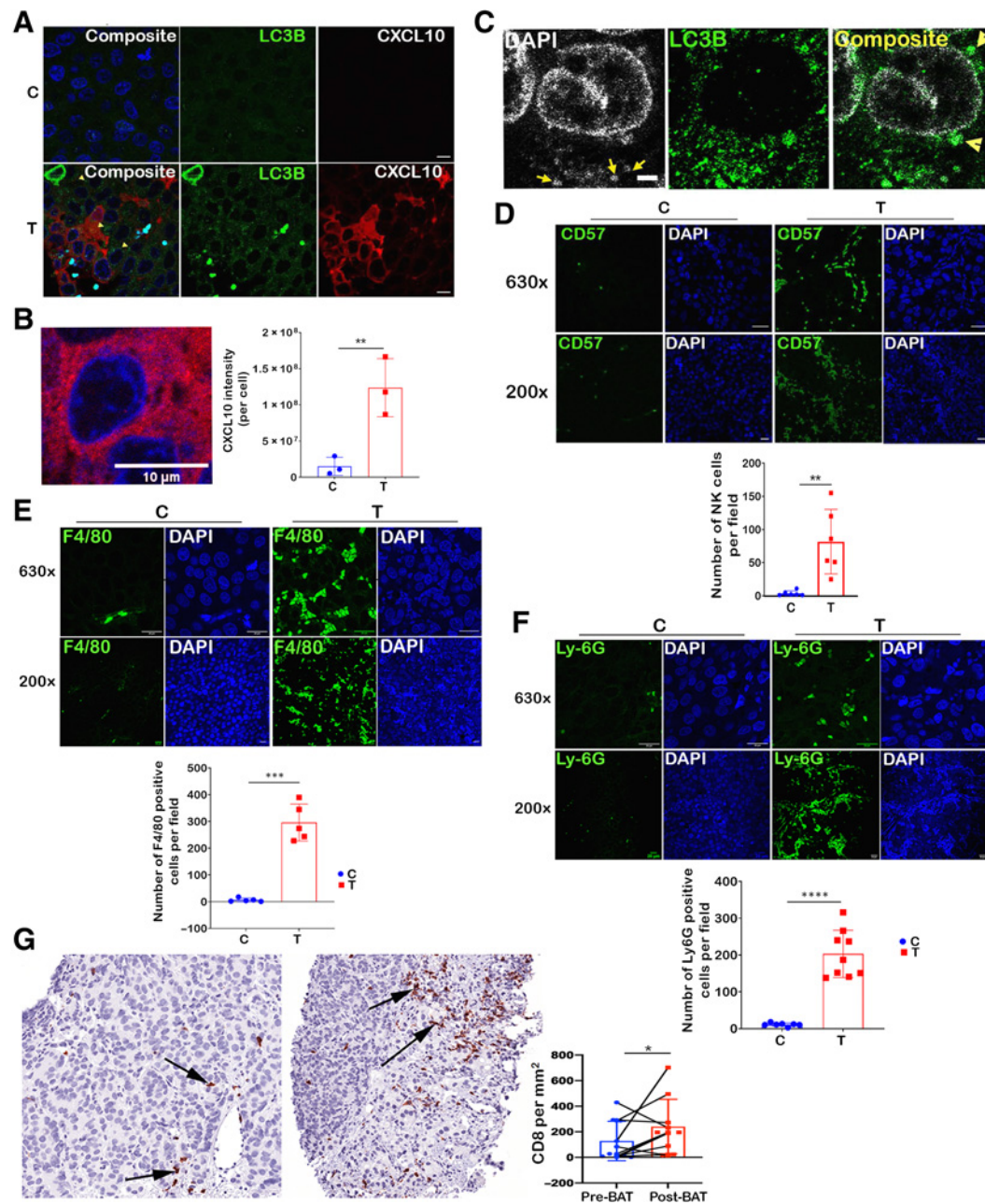
Figure 7.
SupraT induces tumor infiltration of immune cells. **A,** Immunofluorescence staining of tumor xenograft specimens for LC3B (green) and CXCL10 (red) from tumor-bearing mice treated with testosterone cypionate (T; $n = 4$) in the bottom panel as compared with tumor isolated from vehicle (C)-treated animals ($n = 4$) shown in the top. Each sample had at least five random field images. **B,** Magnified view of a tumor cell showing cytoplasmic localization of CXCL10 (red). Bar graph shows CXCL10 measured by analyzing images (at least five fields) on ImageJ in control and testosterone-treated groups. **C,** Tumor xenografts specimens from testosterone cypionate–treated mice stained with DAPI (gray) and LC3B (green) to show the presence of cytoplasmic autophagosomal DNA. **D–F,** At least five random images were collected for each sample. Representative immunofluorescence images for tumor sections from the vehicle (C) ($n = 4$) or testosterone cypionate–treated (T) mice ($n = 4$) stained with Alexafluor488-antiCD57 (**D**), Alexafluor488-antiF4/80 (**E**), and Alexafluor488-antiLy-6G (**F**). The number of stained NK cells, macrophages, and neutrophils were counted using Fiji image analysis software and plotted as mean on histogram. Each sample had at least five random field images. **G,** IHC staining for CD8 in matched biopsy before and during BAT treatment ($n = 10$). The left photomicrograph shows a medium power image of tumor with sparse CD8 cell infiltrates involving tumor; most of the cells seen represent tumor cells. Note an increase in the extent of infiltrate in the treated sample in image on the right. Arrows, CD8-positive T cells. The histogram shows area normalized number of CD8 T cells in biopsies collected from patients with prostate cancer before and after BAT regimen ($n = 10$). An asterisk indicates a statistically significant difference ($P < 0.05$). Scale bars, 10 μm (**A**), 2 μm (**B**), 25 μm (**C**), 20 μm (**D** and **E**). *, $P < 0.05$; **, $P < 0.01$; ***, $P < 0.001$; ****, $P < 0.0001$.

as androgens have been linked to regulating lipid metabolism (43–45). The increased cellular lipids may serve as substrates for the generation of lipid peroxides, leading to ferroptosis. Future work will provide more insights into the role of SupraT-induced lipid metabolism in ferroptosis.

On the basis of our previous experimental and clinical reports that SupraT induces DSBs and extreme responders to BAT therapy harbor DNA repair mutations (6, 11, 46), we speculated that prostate cancer harboring mutations in the DSB repair pathway would be sensitive to SupraT. We were surprised to note that the damaged DNA was shuttled for autophagosomal degradation. Such nucleophagic degradation of damaged DNA has been noted for radiotherapy and chemotherapy (47–49). A key finding of our study is that SupraT induces STING and downstream NFκB-driven immune genes to activate immune infiltration *in vitro*, in animal xenografts, and in patient resected tumors. Our results further provide insights into cross-talk between the canonical and noncanonical NFκB pathways induced by SupraT. Previous studies have shown that the canonical pathway is rapidly induced upon stimulation, while chronic stimulation is required for the noncanonical pathway to become activated (50). Our results indicate that the canonical pathway is induced 48 hours after SupraT administration, which synchronizes with the induction of autophagy. This early induction suggests that the activation of the canonical pathway might not be a direct response to SupraT, but maybe an indirect response to SupraT-mediated nucleophagy. A key question that remains to be addressed is whether autophagy induction occurs in response to the presence of damaged DNA in the cytoplasm or is induced by SupraT irrespective of DNA repair competency. We did not detect a global increase in autophagic proteins like Beclin or ATG12. Moreover, autophagy was not induced in AR-positive SupraT-insensitive LAPC4 or 22Rv1 cells, indicating that autophagy induction may not solely depend on AR status or SupraT treatment. A decrease in autophagy induction upon NCOA4 knockdown in SupraT-treated cells indicated that NCOA4 may play an important role SupraT-mediated autophagy—a feature that requires further investigation. Another noteworthy observation was the induction of both the STING and RIG-I pathways. While STING activation is mediated by non-self and damaged-self cytoplasmic DNA, RIG-I is stimulated by 5′-triphosphorylated short double-stranded RNA (51). Through mechanisms not yet fully understood, RIG-I is also activated by double-stranded DNA (35). We found MDA5, another RNA sensor, was also induced by SupraT. While the contributions of MDA5 to SupraT-mediated innate immune signaling remain to be elucidated, it is likely to play a minor role as double knockouts of STING/RIG-I were sufficient to abrogate NIK stabilization and NFκB signaling.

STING signaling is considered a double-edged sword as chronic STING signaling is considered pro-tumorigenic, while acute STING signaling is considered anti-tumorigenic (52). Our data indicate that STING is acutely induced by SupraT, a feature that may contribute to its antitumor effect. Infiltration of immune cells in tumor xenografts and patient biopsies further indicates that the immune system is engaged upon SupraT administration. This observation has clinical significance as the presence of immune infiltrates is a key parameter and correlates with therapeutic response to immunotherapy (53). Recently, immune checkpoint therapy has been shown to induce ferroptosis in tumor cells (54). Ferroptosis itself may likely potentiate the immune clearance of tumors through the release of damage-associated molecular patterns (23). Understanding the role of ferroptosis in SupraT-induced immune signaling, may provide additional mechanistic insights into cellular immune response. Furthermore, cytokines and chemokine genes induced by the STING-TBK1-NFκB pathway may serve as predictors of therapeutic response in the future. Impending clinical investigations involving the combination of SupraT with immune checkpoint inhibitors may be further informative.

In summary, our findings suggest that SupraT induces two autophagy-mediated pathways, namely ferritinophagy and nucleophagy. While ferritinophagy may induce ferroptosis, consequently leading to cell death, nucleophagy induces innate immune signaling (through nucleic acid sensing-NFκB signaling) and infiltration of immune cells.

Authors' Disclosures

Authors' Contributions

R. Kumar: Data curation, software, formal analysis, validation, investigation, visualization, methodology, writing–original draft. J. Mendonca: Data curation, software, formal analysis, validation, investigation, visualization, methodology, writing–original draft. O. Owoyemi: Software, methodology. K. Boyapati: Investigation, methodology. N. Thomas: Methodology. S. Kanacharoen: Methodology. M. Coffey: Methodology. D. Topiwala: Methodology. C. Gomes: Methodology. B. Ozbek: Software, methodology. T. Jones: Methodology. M. Rosen: Methodology. L. Dong: Methodology. S. Wiens: Methodology. W. Brennen: Formal analysis, methodology, writing–review and editing. J.T. Isaacs: Formal analysis, methodology, writing–review and editing. A.M. De Marzo: Resources, software, methodology, writing–review and editing. M.C. Markowski: Resources, investigation, methodology, writing–review and editing. E.S. Antonarakis: Resources, funding acquisition, investigation, writing–review and editing. D.Z. Qian: Investigation, writing–review and editing. K.J. Pienta: Resources, investigation, writing–review and editing. D.M. Pardoll: Resources, investigation, writing–review and editing. M.A. Carducci: Resources, supervision, investigation, writing–review and editing. S.R. Denmeade: Resources, investigation, writing–review and editing. S.K. Kachhap: Conceptualization, resources, formal analysis, supervision, funding acquisition, investigation, visualization, methodology, writing–review and editing.

Acknowledgments

References

1. Huggins C, Hodges CV. Studies on prostatic cancer. I. The effect of castration, of estrogen and androgen injection on serum phosphatases in metastatic carcinoma of the prostate. CA Cancer J Clin 1972;1:293–7.

2. Harris WP, Mostaghel EA, Nelson PS, Montgomery B. Androgen deprivation therapy: progress in understanding mechanisms of resistance and optimizing androgen depletion. Nat Clin Pract Urol 2009;6:76–85.

3. Linja MJ, Savinainen KJ, Saramaki OR, Tammela TL, Vessella RL, Visakorpi T. Amplification and overexpression of androgen receptor gene in hormone-refractory prostate cancer. Cancer Res 2001;61:3550–5.

4. Taplin ME, Balk SP. Androgen receptor: a key molecule in the progression of prostate cancer to hormone independence. J Cell Biochem 2004;91:483–90.

5. Isaacs JT, D'Antonio JM, Chen S, Antony L, Dalrymple SP, Ndikuyeze GH, et al. Adaptive auto-regulation of androgen receptor provides a paradigm shifting rationale for bipolar androgen therapy (BAT) for castrate resistant human prostate cancer. Prostate 2012;72:1491–505.

6. Schweizer MT, Antonarakis ES, Wang H, Ajiboye AS, Spitz A, Cao H, et al. Effect of bipolar androgen therapy for asymptomatic men with castration-resistant prostate cancer: results from a pilot clinical study. Sci Transl Med 2015;7:269ra2.

7. Haffner MC, Aryee MJ, Toubaji A, Esopi DM, Albadine R, Gurel B, et al. Androgen-induced TOP2B-mediated double-strand breaks and prostate cancer gene rearrangements. Nat Genet 2010;42:668–75.

8. Mani RS, Tomlins SA, Callahan K, Ghosh A, Nyati MK, Varambally S, et al. Induced chromosomal proximity and gene fusions in prostate cancer. Science 2009;326:1230.

9. Chatterjee P, Schweizer MT, Lucas JM, Coleman I, Nyquist MD, Frank SB, et al. Supraphysiological androgens suppress prostate cancer growth through androgen receptor-mediated DNA damage. J Clin Invest 2019;129:4245–60.

10. Teply BA, Antonarakis ES. Treatment strategies for DNA repair-deficient prostate cancer. Expert Rev Clin Pharmacol 2017;10:889–98.

11. Teply BA, Kachhap S, Eisenberger MA, Denmeade SR. Extreme response to high-dose testosterone in BRCA2- and ATM-mutated prostate cancer. Eur Urol 2017;71:499.

12. Markowski MC, Kachhap S, De Marzo AM, Sena LA, Luo J, Denmeade SR, et al. Molecular and clinical characterization of metastatic castration-resistant prostate cancer (mCRPC) patients achieving deep responses to bipolar androgen therapy. Clin Genitourin Cancer 2021;S1558–7673.

13. Lam HM, Nguyen HM, Labrecque MP, Brown LG, Coleman IM, Gulati R, et al. Durable response of enzalutamide-resistant prostate cancer to supraphysiological testosterone is associated with a multifaceted growth suppression and impaired DNA damage response transcriptomic program in patient-derived xenografts. Eur Urol 2020;77:144–55.

14. Robitaille AC, Mariani MK, Fortin A, Grandvaux N. A High resolution method to monitor phosphorylation-dependent activation of IRF3. J Vis Exp 2016; e53723.

15. Sramkoski RM, Pretlow TG 2nd, Giaconia JM, Pretlow TP, Schwartz S, Sy MS, et al. A new human prostate carcinoma cell line, 22Rv1. In Vitro Cell Dev Biol Anim 1999;35:403–9.

16. Dixon SJ, Lemberg KM, Lamprecht MR, Skouta R, Zaitsev EM, Gleason CE, et al. Ferroptosis: an iron-dependent form of nonapoptotic cell death. Cell 2012;149:1060–72.

17. Stockwell BR, Friedmann Angeli JP, Bayir H, Bush AI, Conrad M, Dixon SJ, et al. Ferroptosis: a regulated cell death nexus linking metabolism, redox biology, and disease. Cell 2017;171:273–85.

18. Dixon SJ, Stockwell BR. The role of iron and reactive oxygen species in cell death. Nat Chem Biol 2014;10:9–17.

19. Doll S, Conrad M. Iron and ferroptosis: a still ill-defined liaison. IUBMB Life 2017;69:423–34.

20. Dowdle WE, Nyfeler B, Nagel J, Elling RA, Liu S, Triantafellow E, et al. Selective VPS34 inhibitor blocks autophagy and uncovers a role for NCOA4 in ferritin degradation and iron homeostasis in vivo. Nat Cell Biol 2014;16:1069–79.

21. Mancias JD, Wang X, Gygi SP, Harper JW, Kimmelman AC. Quantitative proteomics identifies NCOA4 as the cargo receptor mediating ferritinophagy. Nature 2014;509:105–9.

22. Naguib YM. A fluorometric method for measurement of peroxyl radical scavenging activities of lipophilic antioxidants. Anal Biochem 1998;265:290–8.

23. Friedmann Angeli JP, Krysko DV, Conrad M. Ferroptosis at the crossroads of cancer-acquired drug resistance and immune evasion. Nat Rev Cancer 2019;19:405–14.

24. Klionsky DJ, Abdelmohsen K, Abe A, Abedin MJ, Abeliovich H, Acevedo Arozena A, et al. Guidelines for the use and interpretation of assays for monitoring autophagy (3rd edition). Autophagy 2016;12:1–222.

25. Burdette DL, Vance RE. STING and the innate immune response to nucleic acids in the cytosol. Nat Immunol 2013;14:19–26.

26. Yin Q, Tian Y, Kabaleeswaran V, Jiang X, Tu D, Eck MJ, et al. Cyclic di-GMP sensing via the innate immune signaling protein STING. Mol Cell 2012;46:735–45.

27. Dobbs N, Burnaevskiy N, Chen D, Gonugunta VK, Alto NM, Yan N. STING activation by translocation from the ER is associated with infection and auto-inflammatory disease. Cell Host Microbe 2015;18:157–68.

28. Saitoh T, Fujita N, Hayashi T, Takahara K, Satoh T, Lee H, et al. Atg9a controls dsDNA-driven dynamic translocation of STING and the innate immune response. Proc Natl Acad Sci U S A 2009;106:20842–6.

29. Schroder K, Muruve DA, Tschopp J. Innate immunity: cytoplasmic DNA sensing by the AIM2 inflammasome. Curr Biol 2009;19:R262–5.

30. Shang G, Zhang C, Chen ZJ, Bai XC, Zhang X. Cryo-EM structures of STING reveal its mechanism of activation by cyclic GMP-AMP. Nature 2019;567:389–93.

31. Brown TR, Rothwell SW, Migeon CJ. Comparison of methyltrienolone and dihydrotestosterone binding and metabolism in human genital skin fibroblasts. J Steroid Biochem 1981;14:1013–22.

32. Kemppainen JA, Lane MV, Sar M, Wilson EM. Androgen receptor phosphorylation, turnover, nuclear transport, and transcriptional activation. Specificity for steroids and antihormones. J Biol Chem 1992;267:968–74.

33. Tokunaga R, Zhang W, Naseem M, Puccini A, Berger MD, Soni S, et al. CXCL9, CXCL10, CXCL11/CXCR3 axis for immune activation–a target for novel cancer therapy. Cancer Treat Rev 2018;63:40–7.

34. Chiappinelli KB, Strissel PL, Desrichard A, Li H, Henke C, Akman B, et al. Inhibiting DNA methylation causes an interferon response in cancer via dsRNA including endogenous retroviruses. Cell 2015;162:974–86.

35. Ablasser A, Bauernfeind F, Hartmann G, Latz E, Fitzgerald KA, Hornung V. RIG-I-dependent sensing of poly(dA:dT) through the induction of an RNA polymerase III-transcribed RNA intermediate. Nat Immunol 2009;10:1065–72.

36. Sheil JM, Gallimore PH, Zimmer SG, Sopori ML. Susceptibility of Adenovirus 2-transformed rat cell lines to natural killer (NK) cells: direct correlation between NK resistance and in vivo tumorigenicity. J Immunol 1984;132:1578–82.

37. Fong L, Carroll P, Weinberg V, Chan S, Lewis J, Corman J, et al. Activated lymphocyte recruitment into the tumor microenvironment following preoperative sipuleucel-T for localized prostate cancer. J Natl Cancer Inst 2014;106:dju268.

38. Vander Griend DJ, Litvinov IV, Isaacs JT. Stabilizing androgen receptor in mitosis inhibits prostate cancer proliferation. Cell Cycle 2007;6:647–51.

39. Roediger J, Hessenkemper W, Bartsch S, Manvelyan M, Huettner SS, Liehr T, et al. Supraphysiological androgen levels induce cellular senescence in human prostate cancer cells through the Src-Akt pathway. Mol Cancer 2014;13:214.

40. Wen S, Niu Y, Lee SO, Chang C. Androgen receptor (AR) positive vs negative roles in prostate cancer cell deaths including apoptosis, anoikis, entosis, necrosis and autophagic cell death. Cancer Treat Rev 2014;40:31–40.

41. Isaacs JT. Antagonistic effect of androgen on prostatic cell death. Prostate 1984;5:545–57.

42. Schlaepfer IR, Rider L, Rodrigues LU, Gijon MA, Pac CT, Romero L, et al. Lipid catabolism via CPT1 as a therapeutic target for prostate cancer. Mol Cancer Ther 2014;13:2361–71.

43. Swinnen JV, Brusselmans K, Verhoeven G. Increased lipogenesis in cancer cells: new players, novel targets. Curr Opin Clin Nutr Metab Care 2006;9:358–65.

44. Suburu J, Chen YQ. Lipids and prostate cancer. Prostaglandins Other Lipid Mediat 2012;98:1–10.

45. Butler LM, Centenera MM, Swinnen JV. Androgen control of lipid metabolism in prostate cancer: novel insights and future applications. Endocr Relat Cancer 2016;23:R219–27.

46. Teply BA, Wang H, Luber B, Sullivan R, Rifkind I, Bruns A, et al. Bipolar androgen therapy in men with metastatic castration-resistant prostate cancer after progression on enzalutamide: an open-label, phase 2, multicohort study. Lancet Oncol 2018;19:76–86.

47. Park YE, Hayashi YK, Bonne G, Arimura T, Noguchi S, Nonaka I, et al. Autophagic degradation of nuclear components in mammalian cells. Autophagy 2009;5:795–804.

48. Eapen VV, Waterman DP, Bernard A, Schiffmann N, Sayas E, Kamber R, et al. A pathway of targeted autophagy is induced by DNA damage in budding yeast. Proc Natl Acad Sci U S A 2017;114:E1158–E67.

49. Deng L, Liang H, Xu M, Yang X, Burnette B, Arina A, et al. STING-dependent cytosolic DNA sensing promotes radiation-induced type I interferon-dependent antitumor immunity in immunogenic tumors. Immunity 2014; 41:843–52.

50. Sun SC. The non-canonical NF-kappaB pathway in immunity and inflammation. Nat Rev Immunol 2017;17:545–58.

51. Rehwinkel J, Gack MU. RIG-I-like receptors: their regulation and roles in RNA sensing. Nat Rev Immunol 2020;20:537–51.

52. Kwon J, Bakhoum SF. The cytosolic DNA-sensing cGAS-STING pathway in cancer. Cancer Discov 2020;10:26–39.

53. Zou W, Wolchok JD, Chen L. PD-L1 (B7-H1) and PD-1 pathway blockade for cancer therapy: mechanisms, response biomarkers, and combinations. Sci Transl Med 2016;8:328rv4.

54. Wang W, Green M, Choi JE, Gijon M, Kennedy PD, Johnson JK, et al. CD8(+) T cells regulate tumour ferroptosis during cancer immunotherapy. Nature 2019; 569:270–4.

CANCER RESEARCH